

Scaling Relations from Sunyaev-Zel'dovich Effect and Chandra X-ray measurements of high-redshift galaxy clusters

Massimiliano Bonamente^{1,2}, Marshall Joy², Samuel J. LaRoque³, John E. Carlstrom^{3,4},
Daisuke Nagai⁵ and Daniel P. Marrone^{6,3}

ABSTRACT

We present Sunyaev-Zel'dovich Effect (SZE) scaling relations for 38 massive galaxy clusters at redshifts $0.14 \leq z \leq 0.89$, observed with both the *Chandra* X-ray Observatory and the centimeter-wave SZE imaging system at the BIMA and OVRO interferometric arrays. An isothermal β -model with central 100 kpc excluded from the X-ray data is used to model the intracluster medium and to measure global cluster properties. For each cluster, we measure the X-ray spectroscopic temperature, SZE gas mass, total mass and integrated Compton- y parameters within r_{2500} . Our measurements are in agreement with the expectations based on a simple self-similar model of cluster formation and evolution. We compare the cluster properties derived from our SZE observations with and without *Chandra* spatial and spectral information and find them to be in good agreement. We compare our results with cosmological numerical simulations, and find that simulations that include radiative cooling, star formation and feedback match well both the slope and normalization of our SZE scaling relations.

Subject headings: galaxies: clusters

1. Introduction

The Sunyaev-Zel'dovich Effect (SZE) is a unique and powerful observational tool for cosmology (for review see Carlstrom et al. 2002). It is a small distortion in the cosmic microwave

¹Department of Physics, University of Alabama, Huntsville, AL 35812

²NASA/Marshall Space Flight Center, Huntsville, AL 35812

³Kavli Institute for Cosmological Physics, Department of Astronomy and Astrophysics, University of Chicago, Chicago, IL 60637

⁴Department of Physics, Enrico Fermi Institute, University of Chicago, Chicago, IL 60637

⁵Theoretical Astrophysics, California Institute of Technology, Mail Code 130-33, Pasadena, CA 91125

⁶Jansky Fellow, National Radio Astronomy Observatory

background (CMB) spectrum caused by scattering of CMB photons off a distribution of high energy electrons in dense structures such as clusters of galaxies (Sunyaev & Zel’dovich 1970, 1972). This effect has a unique property that the signal is independent of redshift, making it particularly well suited for deep cluster surveys (e.g., Holder et al. 2000; Weller et al. 2002). Several SZE survey experiments are currently in progress (Ruhl et al. 2004; Fowler 2004; Kaneko 2006), and are expected to generate a large sample of SZ-selected clusters with masses greater than $\sim 2 \times 10^{14} M_{\odot}$. The resulting large samples of galaxy clusters will enable direct measurements of the evolution of the number density of galaxy clusters as a function of redshift and in principle can provide a powerful constraint on the nature of dark energy (Wang & Steinhardt 1998; Viana & Liddle 1999; Mohr et al. 2000; Haiman et al. 2001).

To utilize the upcoming SZE cluster surveys for cosmological studies, it is important to understand the relation between the SZE observables and the mass of a cluster. If the evolution of clusters is dominated by gravitational processes, a simple model of cluster formation and evolution based on the virial theorem (Kaiser 1986) predicts simple power-law relations between cluster masses and certain integrated cluster properties, including the integrated SZE flux (which is proportional to Y , the integral of the Compton- y parameter over the solid angle of the cluster). Numerical simulations further suggest that Y should be an excellent proxy of cluster mass when measured on sufficiently large scales (e.g., da Silva et al. 2004; Motl et al. 2005; Nagai 2006). These simulations also predict that the slope and redshift evolution of the SZE scaling relations are relatively insensitive to the details of cluster physics, although numerical simulations show that the input cluster physics affects the normalization of the SZE scaling relations (Nagai 2006). It is therefore important to investigate the properties of the SZE scaling relations observationally.

Previous studies have addressed the correlation between the SZE signal and X-ray properties. For instance, Cooray (1999) found a positive correlation between the central SZE decrement and the X-ray luminosity in a sample of 14 clusters. Similarly, McCarthy et al. (2003) detected correlations between the central SZE decrement and X-ray determined mass, temperature, and luminosity for a 22 cluster sample, and Morandi et al. (2007) for a sample of 24 clusters. These studies use data from multiple SZE and X-ray experiments, making systematics more difficult to control, and focus on the relationship between the central values of the SZE signal with the X-ray properties. Recently, Benson et al. (2004) showed that the integrated SZE flux is a more robust observable than the central values of the SZE signal, and found a strong correlation with X-ray temperatures using a sample of 15 clusters obtained by the Sunyaev-Zeldovich Imaging Experiment (SuZIE, Holzapfel et al. 1997; Benson et al. 2003) and X-ray temperatures from the *ASCA* experiment.

This paper is the third in a series of papers combining SZE and *Chandra* X-ray measure-

ments of galaxy clusters to study cosmological properties, following Bonamente et al. (2006) (B2006 hereafter) and LaRoque et al. (2006) (L2006 hereafter). Here we present observational studies of SZE scaling relations for clusters of galaxies. This paper advances the results of previous cluster scaling relation works in several ways. First, we use the largest observational sample yet constructed (38 clusters at redshift $z=0.14\text{--}0.89$). Second, our analysis is based on SZE and X-ray observations obtained using the same instruments: all SZE fluxes are determined using centimeter-wave interferometric data from the BIMA/OVRO SZE imaging experiments (e.g. LaRoque et al. 2003), and all cluster X-ray properties are derived using data from the *Chandra X-ray Observatory*. Finally, our *Chandra* observations have an order of magnitude better spatial resolution than the X-ray data used in previous studies, which greatly improves our ability to identify and exclude compact foreground sources which are superimposed on the cluster X-ray emission.

Throughout the paper, we assume a Λ CDM cosmology with $\Omega_M=0.3$, $\Omega_\Lambda=0.7$ and $h = 0.7$, where h is defined such that $H_0 = 100 h \text{ km s}^{-1} \text{ Mpc}^{-1}$. All uncertainties are at the 68.3% confidence level.

2. Theory of cluster scaling relations

2.1. The virial radius and r_{2500}

In order to establish relationships between mass, SZE flux and other cluster properties, one needs to define a radius out to which all quantities will be calculated. This radius should be physically motivated, reachable with the current X-ray and SZE observations, and equivalent for clusters of different redshift. One candidate is the virial radius. In a Friedman-Robertson-Walker universe, an unperturbed spherical region expands indefinitely, while a perturbed overdense region (the seed of a future cluster) eventually recollapses. When the overdense region collapses under the effect of its own gravity, it is assumed to reach virial equilibrium when the radius is half of that at maximum expansion (Peebles 1980; Lacey & Cole 1993). The ratio of the mean cluster density to the background density at the time of virialization is $\Delta_v = 18\pi^2$ for a universe with critical matter density ($\Omega_M = 1$). For a different cosmology with $\Omega_k = 0$, Bryan & Norman (1998) showed that $\Delta_v \simeq 18\pi^2 + 82x - 39x^2$, where $x = \Omega_{M0}(1+z)^3/E^2(z)$ and $E^2(z) = \Omega_{M0}(1+z)^3 + \Omega_\Lambda + \Omega_{k0}(1+z)^2$, as found from a fit to numerical simulations (Lacey & Cole 1993).

With this characterization of the mean cluster density at time of virialization, the virial radius can be determined as the radius within which the average density of the cluster is Δ_v times the critical density, via

$$\frac{4}{3}\pi\rho_c(z)\Delta_v(z)r_{vir}^3 = M_{tot}(r_{\Delta_v(z)}) \quad (1)$$

in which both $\rho_c(z)$ and $\Delta_v(z)$ are cosmology dependent, and the critical density $\rho_c(z)$ is defined as:

$$\rho_c(z) = \frac{3H_0^2 E(z)^2}{8\pi G}. \quad (2)$$

Unfortunately, the virial radius is usually unreachable with current X-ray and SZE measurements, and one is forced to perform measurements out to a smaller radius. Such a radius (r_Δ) is characterized by the density contrast parameter Δ in place of $\Delta_v(z)$ in Equation 1, and corresponds to a higher average density, $4/3 \cdot \pi\rho_c(z)\Delta \cdot r_\Delta^3 = M_{tot}(r_\Delta)$. We choose a contrast parameter $\Delta = 2500$, corresponding to an average density of 2500 times the critical density at the cluster’s redshift. This choice is motivated by the fact that this is the radius typically reachable with our SZE and X-ray data without any extrapolation of the models (B2006, L2006).¹

2.2. Scaling relations

The hierarchical structure formation theory developed by Kaiser (1986) predicts simple relationships between physical parameters of collapsed structures, known as scaling relations. With the assumptions of hydrostatic equilibrium and of an isothermal distribution for both the dark matter and the cluster gas (e.g., Bryan & Norman 1998), it can be shown that there is a simple relationship between a cluster’s total mass and its gas temperature T_e :

$$T_e \propto M_{tot}^{2/3} E(z)^{2/3} \quad (3)$$

where the mass is calculated out to a radius of mean overdensity Δ , $M_{tot} = M_{tot}(r_\Delta)$. For $f_{gas} \equiv M_{gas}/M_{tot}$, ($M_{gas} = M_{gas}(r_\Delta)$), the expected relationship between the gas mass within r_Δ and the gas temperature is

$$T_e f_{gas}^{2/3} \propto M_{gas}^{2/3} E(z)^{2/3}. \quad (4)$$

¹The use of a constant overdensity factor Δ was shown by Maughan et al. (2006) to give results similar to the case of a variable overdensity factor $\Delta(z) = \Delta(0)[\Delta_v(z)/\Delta_v(0)]$, in which the variable overdensity scales with redshift in order to keep the ratio of two comoving densities constant.

The Compton- y parameter is a measure of the pressure integrated along the line of sight:

$$y = \int_0^\infty \sigma_T n_e \frac{k_B T_e}{m_e c^2} dl \quad (5)$$

One can further integrate the y parameter over the solid angle Ω subtended by the cluster, to obtain the integrated Compton- y parameter:

$$Y \equiv \int_\Omega y d\Omega = \frac{1}{D_A^2} \left(\frac{k_B \sigma_T}{m_e c^2} \right) \int_0^\infty dl \int_A n_e T_e dA \quad (6)$$

where A is the area of the cluster in the plane of the sky. In the context of an isothermal model, Y is proportional to the integral of the electron density n_e over a cylindrical volume, thus

$$Y D_A^2 \propto T_e \int n_e dV = M_{gas} T_e = f_{gas} M_{tot} T_e. \quad (7)$$

In section 5 we consider the effect of integrating gas mass within a spherical volume while determining Y in a cylinder. Using equation 3 we can rewrite equation 7 in terms of either M_{tot} or T_e , or substitute M_{gas}/f_{gas} for M_{tot} , to obtain:

$$\begin{aligned} Y D_A^2 &\propto f_{gas} T_e^{5/2} E(z)^{-1} \\ Y D_A^2 &\propto f_{gas} M_{tot}^{5/3} E(z)^{2/3} \\ Y D_A^2 &\propto f_{gas}^{-2/3} M_{gas}^{5/3} E(z)^{2/3} \end{aligned} \quad (8)$$

Equations 8 are the scaling relations that we investigate observationally in this paper.

3. SZE and *Chandra* X-ray observations of galaxy clusters

3.1. Data

We analyze the SZE and X-ray data observations of 38 clusters in the redshift range $z=0.14$ – 0.89 , observed with the *BIMA* and *OVRO* interferometric arrays and with the *Chandra* X-ray imaging spectrometers. Both data modeling with the isothermal β model and the data themselves are presented in B2006 and L2006, the previous two papers in this series. We refer to L2006 for details on the observations and data modeling, and to Reese et al. (2002) for a detailed illustration of the modeling of the OVRO/BIMA SZE data in the Fourier plane. In the following, we review those aspects of the data modeling and analysis that are relevant to the investigation of the scaling relations.

3.2. Data modeling

The gas density model is based on the spherical β -model (Cavaliere & Fusco-Femiano 1976, 1978), which has the form

$$n_e(r) = n_{e0} \left(1 + \frac{r^2}{r_c^2} \right)^{-3\beta/2},$$

where n_{e0} is the central electron number density, r is the radius from the center of the cluster, r_c is a core radius, and β is a power-law index. When integrated along the line of sight to determine the projected SZE decrement distribution ($\propto n_e$) and X-ray surface brightness ($\propto n_e^2$), this model has the simple analytic forms

$$\Delta T = \Delta T_0 \left(1 + \frac{\theta^2}{\theta_c^2} \right)^{(1-3\beta)/2} \quad (9)$$

$$S_x = S_{x0} \left(1 + \frac{\theta^2}{\theta_c^2} \right)^{(1-6\beta)/2}, \quad (10)$$

where ΔT_0 is the central thermodynamic SZE temperature decrement/increment and θ_c is the angular core radius of the cluster (e.g., Birkinshaw et al. 1991; Reese et al. 2002). This model typically provides a good description of the X-ray surface brightness and SZE decrement profiles out to $\sim r_{2500}$ (e.g., Jones & Forman 1984; Elbaz et al. 1995; Grego et al. 2001; Reese et al. 2002; Ettori et al. 2004). This simple model, however, does not provide a good description of the peaked X-ray surface brightness observed in the center of some clusters. To minimize the systematic bias associated with modeling of cluster cores, we therefore exclude the central 100 kpc from both the spatial and spectral X-ray data, as was done in the previous two papers in this series. The emission-weighted X-ray spectroscopic temperature is also determined by a single-temperature fit to the X-ray spectrum of photons extracted from an annulus between 100 kpc and r_{2500} (L2006). This 100 kpc-cut model was shown to recover the gas masses of simulated clusters with a range of dynamical states to better than 5% accuracy at r_{2500} (L2006) and, when applied to the determination of the Hubble constant, yielded the same results as a more complex non-isothermal model (B2006). Uncertainties associated with the isothermal assumption are included via an additional systematic error described in section 4.1.

Following our earlier analysis methods, we do not model the dark matter distribution, and calculate the total mass directly from the equation of hydrostatic equilibrium (see Equation 11 below). An upcoming paper (Mroczkowski et al. 2008, in preparation) will extend the analysis to use more sensitive data from the *Sunyaev-Zeldovich Array* (Muchovej et al. 2007) and more accurate modeling of the cluster gas, based on the non-isothermal models of Vikhlinin et al. (2006) and Nagai et al. (2007).

3.3. Analysis Methods

Best-fit model parameters and confidence intervals for all model parameters are obtained using a Markov chain Monte Carlo (MCMC) method described in detail by Bonamente et al. (2004) and B2006. L2006 explains the implementation of the likelihood calculation for the 100 kpc-cut model. For each cluster, the Markov chain constrains the parameters S_{x0} , β , θ_c , ΔT_0 , T_e , and abundance (see L2006 for best-fit values). We use the cosmological parameters $h = 0.7$, $\Omega_M = 0.3$ and $\Omega_\Lambda = 0.7$ to calculate each cluster's angular diameter distance D_A (e.g., Carroll et al. 1992).

From these model parameters we calculate r_{2500} and $M_{tot}(r_{2500})$ through the hydrostatic equilibrium equation (e.g., Grego et al. 2001),

$$M_{tot}(r) = \frac{3\beta k T_X}{G\mu m_p} \frac{r^3}{r_c^2 + r^2}, \quad (11)$$

in which μ is the mean molecular weight calculated using the X-ray metallicities and $r_c = \theta_c D_A$. One obtains r_{2500} from the solution of the following equation:

$$\frac{3\beta k T_X}{G\mu m_p} \frac{r_\Delta^3}{r_c^2 + r_\Delta^2} = \frac{4\pi}{3} r_\Delta^3 \Delta \rho_c(z),$$

in which $\rho_c(z)$ is given by Equation 2, $\Delta = 2500$, and the right hand side is just $M_{tot}(r_{2500})$. We then compute the global cluster quantities needed for the analysis of SZE and X-ray scaling relations. The gas mass is computed by integrating the gas density model,

$$M_{gas}(r_{2500}) = 4\pi \mu_e n_{e0} m_p D_A^3 \int_0^{r_{2500}/D_A} \left(1 + \frac{\theta^2}{\theta_c^2}\right)^{-3\beta/2} \theta^2 d\theta, \quad (12)$$

where μ_e is the mean molecular weight of the electrons, and n_{e0} is the central electron density, obtained from the parameters of the β model (L2006, Equation 12).

The integrated y parameter (Y , equation 6) is calculated using the measured SZE decrement ΔT , which is directly proportional to the Compton- y parameter

$$\Delta T = T_{CMB} \cdot f(x) \cdot y.$$

The factor $f(x)$ is the frequency dependence of the SZE:

$$f(x) = \left(x \cdot \coth\left(\frac{x}{2}\right) - 4\right) \cdot (1 + \delta_{rel}),$$

in which $x = h\nu/k_B T_{CMB}$, and δ_{rel} is a small relativistic correction factor. At our observing frequencies, $f(x) \simeq -2$. Thus,

$$Y = \int_A \frac{\Delta T}{T_{CMB} f(x)} d\Omega = \frac{\Delta T_o}{T_{CMB} f(x)} \int_0^{r_{2500}/D_A} \left(1 + \frac{\theta^2}{\theta_c^2}\right)^{(1-3\beta)/2} \theta d\theta. \quad (13)$$

4. Observational constraints on SZE scaling relations

4.1. Regression method

Our measurements of masses and integrated y parameters, using the method described in Section 3, are shown in Table 1. The errors in Table 1 represent the photon-counting statistical uncertainties of the X-ray data and the statistical uncertainties of the SZE observations. Additional sources of uncertainty in the measurement of cluster parameters include cluster asphericity and projection effects, small-scale clumping of the gas, the presence of point sources in the field, CMB anisotropy, the assumption of isothermality, and instrumental calibration, as discussed by Reese et al. (2002), L2006, and B2006. Therefore, in fitting Y versus T_X , M_{gas} , and M_{tot} (Equations 8), we include an additional statistical error (combined in quadrature) of $\pm 20\%$ for the masses, and $\pm 10\%$ for Y and T_X .

We perform a linear least-squares regression in log space, $\log(Y) = A + B \cdot \log(X)$, following the method of Press et al. (1992) and Benson et al. (2004). This method accounts for errors in both measured parameters for each scaling relation, and it minimizes the χ^2 statistic defined as

$$\chi^2 = \sum \frac{(\log(Y_i) - A - B\log(X_i))^2}{\sigma_{\log(Y_i)}^2 + (B\sigma_{\log(X_i)})^2}$$

in which $\sigma_{\log(Y_i)} = \sigma_{Y_i}/Y_i \log(e)$, $\sigma_{\log(X_i)} = \sigma_{X_i}/X_i \log(e)$, and the linear errors σ_{Y_i} and σ_{X_i} are obtained from the upper and lower uncertainties around the best-fit values as $\sigma = (\sigma^+ + \sigma^-)/2$.

4.2. The Y - M_{gas} , Y - M_{tot} and Y - kT scaling relations

The above derivation of the self-similar scaling relations does not include any variation of the gas fraction with cluster mass. However, there may be some evidence for such variation in both X-ray observations (e.g., Vikhlinin et al. 2006) and simulations (Kravtsov et al. 2005). We examine this in the present data by performing a logarithmic fit to the f_{gas} - M_{gas} data using a linear relationship ($\log(Y) = A + B\log(X)$). We find no significant evidence for a variation of f_{gas} with mass ($B = 0.14 \pm 0.08$). In the following we therefore assume that f_{gas} is a constant. We then perform similar logarithmic fits to the Y - M_{gas} , Y - M_{tot} and Y - kT data. The results are shown in Figure 2 and in Table 2. Under the assumption of a constant f_{gas} , all scaling relations are consistent (within 2σ statistical uncertainty) with the simple self-similar model of cluster evolution.

4.3. Redshift evolution of the Y - M_{gas} , Y - M_{tot} and Y - kT scaling relations

The large number of clusters (38) and redshift coverage of our *Chandra* and *OVRO-BIMA* data ($0.14 \leq z \leq 0.89$) enables the investigation of a possible redshift evolution of the SZE scaling relations. For this purpose, we divide our sample evenly into low-redshift clusters ($z \leq 0.30$, 19 clusters) and high-redshift clusters ($0.30 < z \leq 0.89$, 19 clusters), and repeat the logarithmic fits of Section 4.2.

The results of Table 2 indicate no evidence for redshift evolution of the SZE scaling relations, as f_{gas} is consistent with a constant for both low and high-redshift clusters. Furthermore, the SZE scaling relations are consistent with the self-similar slopes at or below the 2.5σ level.

5. Comparison of SZE and X-ray Measurements

In the previous section we have examined the SZE scaling relations based on quantities derived jointly from SZE and X-ray observations. Here we compare the cluster properties derived from our SZE observations without using the X-ray data in the fits, in order to determine whether the relations we observe depend strongly on the X-ray information.

We analyze the SZE data using the model of Section 3.2, using additional assumptions to provide the constraints that would otherwise be provided by the X-ray data. As a first assumption we fix $\beta = 0.7$ and fit for θ_c and ΔT_0 in Equation 9, following L2006. The choice of fixing $\beta = 0.7$ is determined by the fact that this is the median value for our sample; L2006 also show that using values of 0.6 and 0.8 results in changes to the parameters that are small relative to the 68% statistical uncertainties. The data quality allows us to perform this SZE-only analysis for 25 of the clusters in the full sample, as shown in Table 3. Knowledge of the gas temperature is required in order to determine r_{2500} , as can be seen from the combination of Equations 1 and 11:

$$r_{2500} = \sqrt{\left(\frac{3\beta kT}{G\mu m_p}\right) \frac{1}{\frac{4}{3}\pi\rho_c(z) \cdot 2500} - r_c^2}.$$

In the absence of complementary X-ray spectroscopic data, we estimate the gas temperature directly from the SZE data following the iterative method described by Joy et al. (2001). We first choose an initial estimate of the gas temperature, from which we obtain r_{2500} and $M_{tot}(r_{2500})$. We derive $M_{gas}(r_{2500})$ using the equations described in Section 3.3, with the central gas density n_{e0} calculated from the parameters of the SZE decrement model (L2006, Equation 13). We provide a final constraint by assuming that the gas mass fraction of each

cluster is equal to the average value for this sample, $f_{gas} = 0.116$ (L2006), and iteratively solve the equation $M_{gas}(r_{2500}) = f_{gas} \cdot M_{tot}(r_{2500})$ in order to find self-consistent estimates of T and r_{2500} .

Results of the SZE analysis are shown in Table 3. In Figure 3 we compare the SZE measurements of gas temperature, r_{2500} , Y , and gas mass with the values from the joint analysis of Section 3. In the joint analysis, the X-ray data are solely responsible for the measurement of the temperature, and drive the fit of the spatial parameters and gas density. They therefore drive the measurements of r_{2500} and M_{gas} as well. The quantities inferred from the SZE data are in good agreement with those from the joint analysis, indicating that we have not altered the scaling relations of Section 4.2 by incorporating the X-ray data. Although these results show that it is possible to estimate Y and the cluster gas mass from the SZE data alone, the joint analysis is preferred because it provides the strongest constraints on cluster properties, requires fewer assumptions about the cluster structure and composition, and can be applied to the full 38-cluster sample. Nevertheless, the ability to derive cluster properties from SZE observations will be important for the many SZE cluster surveys currently underway (Ruhl et al. 2004; Fowler 2004; Kaneko 2006); these surveys are expected to generate large samples of SZE-selected clusters but will not generally have access to deep X-ray observations for cluster characterization. The gas temperature may also be inferred from multi-frequency SZE observations (Hansen et al. 2002).

Recent work by Kravtsov et al. (2006) indicate that the quantity $Y_X \equiv M_{gas} \cdot k_B T_e$, the X-ray analogue of Y , is a low-scatter proxy for the cluster total mass. For the isothermal β -model used in this paper, the gas mass can be estimated from X-ray data by using Equation 12, and thus our data also provide a measurement of Y_X . We can therefore compare Y with Y_X , in order to establish observationally whether the two quantities are indeed equivalent. In the case of the isothermal β -model, the integrated Compton- y parameter is an integral of the electron density over a cylinder \mathcal{C} of infinite length along the line of sight, and of area $A = \pi r_{2500}^2$:

$$Y D_A^2 = \left(\frac{k_B \sigma_T T_e}{m_e c^2} \right) \int_{\mathcal{C}} n_e(r) dV = \left(\frac{k_B \sigma_T T_e}{m_e c^2} \right) \frac{1}{m_p \mu_e} \int_{\mathcal{C}} n_e m_p \mu_e dV.$$

Since the gas mass is given by an integral over a sphere \mathcal{S} of radius r_{2500} ,

$$M_{gas} = \int_{\mathcal{S}} n_e m_p \mu_e dV$$

the relationship between Y and Y_X is

$$Y D_A^2 = \left(\frac{\sigma_T}{m_e c^2} \right) \frac{1}{m_p \mu_e} C Y_X \tag{14}$$

where the constant $C = \int_C n_e dV / \int_S n_e dV$ accounts for the different domain of integration of Y and Y_X , and depends on the parameters of the β model. We calculate C separately for each cluster, and typically find $C \sim 2$.

In Figure 4 we plot Y , as derived from the joint SZE/X-ray analysis, against Y_X . A fit of the data to the relationship in Equation 14 (the dotted line in Figure 4, with no degrees of freedom) results in an acceptable χ^2 statistic, corresponding to a null hypothesis probability of 80.4%. The agreement with the relationship in Equation 14 shows that Y_X is an unbiased estimator of the integrated Compton- y parameter, within the uncertainties of the current measurements.

6. Comparison with theoretical simulations

We compare our results with those of recent cosmological cluster simulations (Nagai 2006; Nagai et al. 2007) that include radiative cooling, UV heating, star formation, and stellar feedback processes in addition to the standard gas dynamics. In Figure 5 we compare 16 clusters simulated at $z=0$ and 0.6 using cooling and star formation feedback processes (in red), the same sets of clusters performed using non-radiative gas dynamics (in green), and our 38 clusters observed with *Chandra* and OVRO-BIMA (in black).

The best-fit power-law models that describe the two simulations are shown as dashed lines in Figure 5. A fit of our data to the cooling and star formation model (red dashed line) results in a χ^2 null hypothesis probability of 99.9%, and the non-radiative model (green dashed line) has a probability of 0.5%. The comparison indicates that both simulation models show a similar slope to the observed clusters, with the cooling and star formation feedback model providing a better match to the data.

7. Discussion and conclusions

We have investigated scaling relations between the integrated Compton- y parameter Y and total mass, gas mass, and gas temperature using 38 clusters observed with *Chandra* and *OVRO-BIMA*. Fits of the Y - M_{gas} , Y - M_{tot} and Y - kT data to a power-law model agree with the slope predicted by a self-similar model in which the evolution of clusters is dominated by gravitational processes. The normalization of the Y - M_{gas} scaling relation agrees well with the numerical simulations of Nagai et al. (2007), in which collisionless dynamics of dark matter and gas dynamics are complemented by cooling, star formation and feedback phenomena. The agreement provides observational evidence that non-gravitational phenomena may also

be an important factor in the physics of clusters.

The redshift coverage of our sample enabled an analysis of the scaling relations as function of redshift, by defining a low redshift sample ($0.14 \leq z \leq 0.30$, 19 clusters) and a high-redshift sample ($0.30 < z \leq 0.89$, 19 clusters). Both samples follow the prediction based on the self-similar model. Our data indicate no significant evolution in the SZE properties of clusters at redshift $z \lesssim 1$.

We also measure the cluster mass and integrated Y parameter using the SZE data alone, without making use of the *Chandra* spectral and spatial information. These measurements are in good agreement with those based on the joint X-ray/SZE analysis, providing evidence that SZE surveys can be used to determine the number density of galaxy clusters as functions of mass and redshift.

This work was made possible by the skill and dedication of Leon van Speybroeck and his colleagues on the Chandra project, who constructed an exceptional observatory and obtained deep X-ray observations for a large sample of galaxy clusters. We thank E. Leitch and the anonymous referee for excellent suggestions on the manuscript. The support of the BIMA and OVRO staff over many years is also gratefully acknowledged, including J.R. Forster, C. Giovanine, R. Lawrence, S. Padin, R. Plambeck, S. Scott and D. Woody. We thank C. Alexander, K. Coble, A. Cooray, K. Dawson, L. Grego, G. Holder, W. Holzappel, A. Miller, J. Mohr, S. Patel, E. Reese, and P. Whitehouse for their outstanding contributions to the SZE instrumentation, observations, and analysis.

This work was supported in part by NSF grants AST-0096913 and AST-0604982 and by the KICP NSF Physics Frontier Center grant PHY-0114422. Research at the Owens Valley Radio Observatory and the Berkeley-Illinois-Maryland Array was supported by National Science Foundation grants AST 99-81546 and 02-28963. Calculations were performed at the Space Plasma Interactive Data Analysis and Simulation Laboratory at the Center for Space Plasma and Aeronomy Research of the University of Alabama at Huntsville. DN is supported by the Sherman Fairchild Postdoctoral Fellowship at Caltech. The National Radio Astronomy Observatory is a facility of the National Science Foundation operated under cooperative agreement by Associated Universities, Inc.

REFERENCES

Benson, B. A., Church, S. E., Ade, P. A. R., Bock, J. J., Ganga, K. M., Henson, C. N., & Thompson, K. L. 2004, ApJ, 617, 829

- Benson, B. A. et al. 2003, *ApJ*, 592, 674
- Birkinshaw, M., Hughes, J. P., & Arnaud, K. A. 1991, *ApJ*, 379, 466
- Bonamente, M., Joy, M. K., Carlstrom, J. E., Reese, E. D., & LaRoque, S. J. 2004, *ApJ*, 614, 56
- Bonamente, M., Joy, M. K., LaRoque, S. J., Carlstrom, J. E., Reese, E. D., & Dawson, K. S. 2006, *ApJ*, 647, 25
- Bryan, G. L., & Norman, M. L. 1998, *ApJ*, 495, 80
- Carlstrom, J. E., Holder, G. P., & Reese, E. D. 2002, *ARA&A*, 40, 643
- Carroll, S. M., Press, W. H., & Turner, E. L. 1992, *ARA&A*, 30, 499
- Cavaliere, A., & Fusco-Femiano, R. 1976, *A&A*, 49, 137
- . 1978, *A&A*, 70, 677
- Cooray, A. R. 1999, *MNRAS*, 307, 841
- da Silva, A. C., Kay, S. T., Liddle, A. R., & Thomas, P. A. 2004, *MNRAS*, 348, 1401
- Elbaz, D., Arnaud, M., & Böhringer, H. 1995, *A&A*, 293, 337
- Ettori, S., Tozzi, P., Borgani, S., & Rosati, P. 2004, *A&A*, 417, 13
- Fowler, J. W. 2004, in Presented at the Society of Photo-Optical Instrumentation Engineers (SPIE) Conference, Vol. 5498, Millimeter and Submillimeter Detectors for Astronomy II. Edited by Jonas Zmuidzinas, Wayne S. Holland and Stafford Withington Proceedings of the SPIE, Volume 5498, pp. 1-10 (2004)., ed. C. M. Bradford, P. A. R. Ade, J. E. Aguirre, J. J. Bock, M. Dragovan, L. Duband, L. Earle, J. Glenn, H. Matsuhara, B. J. Naylor, H. T. Nguyen, M. Yun, & J. Zmuidzinas, 1–10
- Grego, L., Carlstrom, J. E., Reese, E. D., Holder, G. P., Holzzapfel, W. L., Joy, M. K., Mohr, J. J., & Patel, S. 2001, *ApJ*, 552, 2
- Haiman, Z., Mohr, J. J., & Holder, G. P. 2001, *ApJ*, 553, 545
- Hansen, S. H., Pastor, S., & Semikoz, D. V. 2002, *ApJ*, 573, L69
- Holder, G. P., Mohr, J. J., Carlstrom, J. E., Evrard, A. E., & Leitch, E. M. 2000, *ApJ*, 544, 629
- Holzzapfel, W. L., Wilbanks, T. M., Ade, P. A. R., Church, S. E., Fischer, M. L., Mauskopf, P. D., Osgood, D. E., & Lange, A. E. 1997, *ApJ*, 479, 17
- Jones, C., & Forman, W. 1984, *ApJ*, 276, 38
- Joy, M. et al. 2001, *ApJ*, 551, L1
- Kaiser, N. 1986, *MNRAS*, 222, 323
- Kaneko, T. 2006, in Presented at the Society of Photo-Optical Instrumentation Engineers (SPIE) Conference, Vol. 6267, Ground-based and Airborne Telescopes. Edited by Stepp, Larry M.. Proceedings of the SPIE, Volume 6267, pp. 62673R (2006).
- Kravtsov, A. V., Nagai, D., & Vikhlinin, A. A. 2005, *ApJ*, 625, 588
- Kravtsov, A. V., Vikhlinin, A., & Nagai, D. 2006, *ApJ*, 650, 128
- Lacey, C., & Cole, S. 1993, *MNRAS*, 262, 627

- LaRoque, S. J., Bonamente, M., Carlstrom, J. E., Joy, M. K., Nagai, D., Reese, E. D., & Dawson, K. S. 2006, *ApJ*, 652, 917
- LaRoque, S. J. et al. 2003, *ApJ*, 583, 559
- Maughan, B. J., Jones, L. R., Ebeling, H., & Scharf, C. 2006, *MNRAS*, 365, 509
- McCarthy, I. G., Holder, G. P., Babul, A., & Balogh, M. L. 2003, *ApJ*, 591, 526
- Mohr, J. J., Haiman, Z., & Holder, G. P. 2000, *astro-ph/0004244*
- Morandi, A., Ettori, S., & Moscardini, L. 2007, *ArXiv e-prints*, 704
- Motl, P. M., Hallman, E. J., Burns, J. O., & Norman, M. L. 2005, *ApJ*, 623, L63
- Muchovej, S. et al. 2007, *ApJ*, 663, 708
- Nagai, D. 2006, *ApJ*, 650, 538
- Nagai, D., Kravtsov, A. V., & Vikhlinin, A. 2007, *ApJ*, 668, 1
- Peebles, P. J. E. 1980, *The Large-scale Structure of the Universe* (Princeton University Press)
- Press, W. H., Teukolsky, S. A., Vetterling, W. T., & Flannery, B. P. 1992, *Numerical Recipes in C. The Art of Scientific Computing* (Cambridge University Press, 2nd ed.)
- Reese, E. D., Carlstrom, J. E., Joy, M., Mohr, J. J., Grego, L., & Holzappel, W. L. 2002, *ApJ*, 581, 53
- Ruhl, J. E. et al. 2004, *astro-ph/0411122*
- Sunyaev, R. A., & Zel'dovich, Y. B. 1970, *Comments Astrophys. Space Phys.*, 2, 66
- . 1972, *Comments Astrophys. Space Phys.*, 4, 173
- Viana, P. T. P., & Liddle, A. R. 1999, *MNRAS*, 303, 535
- Vikhlinin, A., Kravtsov, A., Forman, W., Jones, C., Markevitch, M., Murray, S. S., & Van Speybroeck, L. 2006, *ApJ*, 640, 691
- Wang, L., & Steinhardt, P. J. 1998, *ApJ*, 508, 483
- Weller, J., Battye, R. A., & Kneissl, R. 2002, *Physical Review Letters*, 88, 231301

Table 1. Cluster Parameters from Joint Analysis of X-ray and SZE Data

Cluster	z	D_A (Gpc)	$E(z)$	r_{2500} ($''$)	r_{2500} (kpc)	kT (keV)	M_{gas} ($10^{13}M_{\odot}$)	M_{tot} ($10^{14}M_{\odot}$)	Y (mJy)	f_{gas}
Abell 1413	0.14	0.52	1.07	206 \pm 10	519 \pm 14	7.5 \pm 0.4	2.6 \pm 0.1	2.2 \pm 0.2	2.99 \pm 0.44	0.120 \pm 0.004
Abell 1689	0.18	0.63	1.09	219 \pm 17	664 \pm 16	10.5 \pm 0.5	5.1 \pm 0.2	5.0 \pm 0.4	3.79 \pm 0.34	0.102 \pm 0.004
Abell 1835	0.25	0.81	1.13	172 \pm 20	672 \pm 20	11.4 \pm 0.7	5.8 \pm 0.2	5.6 \pm 0.5	2.09 \pm 0.17	0.104 \pm 0.005
Abell 1914	0.17	0.60	1.09	228 \pm 15	660 \pm 15	9.5 \pm 0.4	4.8 \pm 0.1	4.8 \pm 0.3	3.01 \pm 0.25	0.101 \pm 0.003
Abell 1995	0.32	0.96	1.18	133 \pm 21	621 \pm 22	8.2 \pm 0.4	3.5 \pm 0.1	4.7 \pm 0.5	0.75 \pm 0.05	0.074 \pm 0.005
Abell 2111	0.23	0.76	1.12	141 \pm 10	518 \pm 36	8.2 \pm 1.0	2.2 \pm 0.3	2.5 \pm 0.6	0.95 \pm 0.21	0.088 \pm 0.008
Abell 2163	0.20	0.68	1.10	206 \pm 10	682 \pm 10	14.8 \pm 0.4	8.1 \pm 0.2	5.5 \pm 0.2	6.89 \pm 0.20	0.147 \pm 0.003
Abell 2204	0.15	0.54	1.08	256 \pm 13	671 \pm 34	11.2 \pm 0.8	4.7 \pm 0.3	5.0 \pm 0.8	4.43 \pm 0.50	0.096 \pm 0.009
Abell 2218	0.18	0.63	1.09	191 \pm 18	581 \pm 18	7.8 \pm 0.4	3.0 \pm 0.1	3.3 \pm 0.6	1.94 \pm 0.18	0.090 \pm 0.004
Abell 2259	0.16	0.57	1.08	172 \pm 22	476 \pm 23	5.8 \pm 0.4	1.8 \pm 0.1	1.8 \pm 0.2	0.82 \pm 0.30	0.101 \pm 0.007
Abell 2261	0.22	0.73	1.12	148 \pm 19	525 \pm 22	7.4 \pm 0.5	3.0 \pm 0.1	2.6 \pm 0.3	1.34 \pm 0.16	0.119 \pm 0.008
Abell 267	0.23	0.76	1.12	132 \pm 7	484 \pm 31	5.9 \pm 0.7	2.2 \pm 0.2	2.0 \pm 0.3	0.72 \pm 0.10	0.110 \pm 0.011
Abell 370	0.38	1.07	1.22	97 \pm 4	508 \pm 21	8.7 \pm 0.5	2.8 \pm 0.2	2.8 \pm 0.4	0.71 \pm 0.09	0.100 \pm 0.005
Abell 586	0.17	0.60	1.09	182 \pm 23	529 \pm 23	6.4 \pm 0.5	2.3 \pm 0.1	2.5 \pm 0.3	1.03 \pm 0.14	0.091 \pm 0.007
Abell 611	0.29	0.90	1.16	111 \pm 17	482 \pm 16	6.8 \pm 0.4	2.4 \pm 0.1	2.1 \pm 0.2	0.54 \pm 0.06	0.111 \pm 0.006
Abell 665	0.18	0.63	1.09	162 \pm 15	490 \pm 10	8.4 \pm 0.4	2.6 \pm 0.1	2.0 \pm 0.1	2.68 \pm 0.06	0.131 \pm 0.004
Abell 68	0.26	0.83	1.14	153 \pm 10	616 \pm 40	9.6 \pm 1.1	3.6 \pm 0.3	4.3 \pm 0.9	1.01 \pm 0.16	0.084 \pm 0.009
Abell 697	0.28	0.88	1.15	134 \pm 31	568 \pm 21	10.2 \pm 0.7	4.4 \pm 0.3	3.5 \pm 0.4	1.67 \pm 0.19	0.126 \pm 0.006
Abell 773	0.22	0.73	1.12	148 \pm 19	527 \pm 20	8.2 \pm 0.6	2.7 \pm 0.2	2.6 \pm 0.3	1.68 \pm 0.19	0.106 \pm 0.005
CL J0016+1609	0.54	1.31	1.34	80 \pm 5	507 \pm 19	10.5 \pm 0.6	4.4 \pm 0.3	3.3 \pm 0.4	0.73 \pm 0.06	0.131 \pm 0.007
CL J1226+3332	0.89	1.60	1.65	66 \pm 5	512 \pm 58	13.5 \pm 2.2	3.9 \pm 0.5	5.2 \pm 2.0	0.35 \pm 0.05	0.075 \pm 0.015
MACS J0647.7+7015	0.58	1.36	1.37	92 \pm 4	606 \pm 41	14.1 \pm 1.8	4.9 \pm 0.5	6.0 \pm 1.3	0.62 \pm 0.08	0.082 \pm 0.009
MACS J0744.8+3927	0.69	1.47	1.47	59 \pm 3	420 \pm 35	8.1 \pm 0.7	3.1 \pm 0.2	2.3 \pm 0.4	0.34 \pm 0.04	0.136 \pm 0.012
MACS J1149.5+2223	0.54	1.31	1.34	71 \pm 4	449 \pm 25	9.9 \pm 0.8	3.1 \pm 0.2	2.3 \pm 0.4	0.58 \pm 0.07	0.134 \pm 0.008
MACS J1311.0-0310	0.49	1.25	1.30	74 \pm 7	448 \pm 46	7.2 \pm 1.1	2.1 \pm 0.2	2.2 \pm 0.5	0.28 \pm 0.05	0.097 \pm 0.017
MACS J1423.8+2404	0.55	1.32	1.35	66 \pm 14	422 \pm 14	7.0 \pm 0.4	2.3 \pm 0.1	1.9 \pm 0.2	0.28 \pm 0.05	0.116 \pm 0.006
MACS J2129.4-0741	0.57	1.35	1.36	73 \pm 30	474 \pm 27	8.6 \pm 0.8	3.3 \pm 0.3	2.8 \pm 0.5	0.39 \pm 0.05	0.116 \pm 0.011
MACS J2214.9-1359	0.48	1.23	1.29	91 \pm 30	547 \pm 30	10.2 \pm 1.0	3.9 \pm 0.3	3.9 \pm 0.7	0.77 \pm 0.09	0.102 \pm 0.009
MACS J2228.5+2036	0.41	1.12	1.24	81 \pm 28	444 \pm 22	8.4 \pm 0.9	2.8 \pm 0.2	2.0 \pm 0.3	0.94 \pm 0.11	0.138 \pm 0.009
MS 0451.6-0305	0.55	1.32	1.35	82 \pm 23	526 \pm 23	9.9 \pm 0.8	4.8 \pm 0.3	3.8 \pm 0.5	0.66 \pm 0.05	0.128 \pm 0.009
MS 1054.5-0321	0.83	1.57	1.59	89 \pm 10	686 \pm 106	9.8 \pm 1.1	7.4 \pm 1.0	4.5 \pm 1.2	0.77 \pm 0.11	0.164 \pm 0.019
MS 1137.5+6625	0.78	1.54	1.55	42 \pm 5	311 \pm 25	4.5 \pm 0.5	1.2 \pm 0.1	1.0 \pm 0.3	0.09 \pm 0.01	0.115 \pm 0.013
MS 1358.4+6245	0.33	0.98	1.19	113 \pm 33	539 \pm 28	8.9 \pm 0.9	3.1 \pm 0.2	3.1 \pm 0.5	0.56 \pm 0.08	0.081 \pm 0.006
MS 2053.7-0449	0.58	1.36	1.37	54 \pm 5	358 \pm 34	4.8 \pm 0.7	0.9 \pm 0.1	1.2 \pm 0.4	0.09 \pm 0.02	0.076 \pm 0.011
RX J1347.5-1145	0.45	1.19	1.27	122 \pm 4	706 \pm 22	16.5 \pm 1.0	8.8 \pm 0.4	8.1 \pm 0.8	1.62 \pm 0.18	0.109 \pm 0.006
RX J1716.4+6708	0.81	1.56	1.57	45 \pm 3	341 \pm 33	6.6 \pm 0.9	1.2 \pm 0.2	1.4 \pm 0.4	0.10 \pm 0.03	0.088 \pm 0.013
RX J2129.7+0005	0.24	0.78	1.13	128 \pm 4	486 \pm 20	6.7 \pm 0.5	2.6 \pm 0.2	2.1 \pm 0.3	0.66 \pm 0.02	0.124 \pm 0.008
ZW 3146	0.29	0.90	1.16	132 \pm 3	574 \pm 11	8.3 \pm 0.3	4.4 \pm 0.1	3.6 \pm 0.2	0.88 \pm 0.10	0.122 \pm 0.004

Table 2. Scaling Relations from Joint Analysis of X-ray and SZE Data

Scaling relation	All clusters		$0.14 \leq z \leq 0.30$		$0.31 < z \leq 0.89$	
	A	B	A	B	A	B
f_{gas}, M_{gas}	-2.86 \pm 1.09	0.14 \pm 0.08	-2.60 \pm 1.79	0.12 \pm 0.13	-3.00 \pm 1.37	0.15 \pm 0.10
Y, kT	-6.24 \pm 0.22	2.37 \pm 0.23	-6.33 \pm 0.32	2.46 \pm 0.34	-6.13 \pm 0.30	2.27 \pm 0.30
Y, M_{gas}	-23.25 \pm 1.77	1.41 \pm 0.13	-25.86 \pm 3.45	1.60 \pm 0.25	-21.43 \pm 3.00	1.28 \pm 0.15
Y, M_{tot}	-28.23 \pm 3.00	1.66 \pm 0.20	-31.20 \pm 5.35	1.87 \pm 0.35	-25.45 \pm 3.46	1.47 \pm 0.23

Table 3. Cluster Parameters from Analysis of SZE Data

Cluster	z	r_{2500} (")	kT (keV)	M_{gas} ($10^{13} M_{\odot}$)	M_{tot} ($10^{14} M_{\odot}$)	Y (10^{-10})
Abell 1689.....	0.18	196^{+8}_{-8}	$8.0^{+0.8}_{-0.7}$	$4.2^{+0.6}_{-0.5}$	$3.6^{+0.5}_{-0.4}$	$1.88^{+0.49}_{-0.38}$
Abell 1835.....	0.25	169^{+5}_{-5}	$11.4^{+1.0}_{-0.9}$	$6.1^{+0.6}_{-0.6}$	$5.3^{+0.5}_{-0.5}$	$2.66^{+0.60}_{-0.48}$
Abell 1914.....	0.17	212^{+10}_{-9}	$8.5^{+1.0}_{-0.8}$	$4.5^{+0.7}_{-0.6}$	$3.9^{+0.6}_{-0.5}$	$2.39^{+0.77}_{-0.54}$
Abell 1995.....	0.32	117^{+3}_{-3}	$8.4^{+0.6}_{-0.6}$	$3.7^{+0.3}_{-0.3}$	$3.2^{+0.3}_{-0.3}$	$0.84^{+0.16}_{-0.14}$
Abell 2111.....	0.23	124^{+9}_{-9}	$5.4^{+1.6}_{-1.0}$	$2.0^{+0.5}_{-0.4}$	$1.7^{+0.4}_{-0.3}$	$0.45^{+0.36}_{-0.18}$
Abell 2163.....	0.20	229^{+13}_{-12}	$15.6^{+2.4}_{-2.0}$	$8.7^{+1.6}_{-1.3}$	$7.5^{+1.4}_{-1.2}$	$8.03^{+3.16}_{-2.26}$
Abell 2218.....	0.18	206^{+12}_{-11}	$10.0^{+1.5}_{-1.3}$	$4.8^{+0.9}_{-0.8}$	$4.1^{+0.8}_{-0.6}$	$3.20^{+1.24}_{-0.90}$
Abell 2261.....	0.22	146^{+10}_{-8}	$6.4^{+1.0}_{-0.8}$	$2.9^{+0.6}_{-0.5}$	$2.5^{+0.5}_{-0.4}$	$0.76^{+0.34}_{-0.21}$
Abell 267.....	0.23	138^{+7}_{-7}	$6.5^{+1.0}_{-0.8}$	$2.7^{+0.4}_{-0.4}$	$2.3^{+0.4}_{-0.3}$	$0.75^{+0.30}_{-0.21}$
Abell 370.....	0.38	96^{+4}_{-3}	$7.3^{+0.8}_{-0.7}$	$3.0^{+0.3}_{-0.3}$	$2.6^{+0.3}_{-0.3}$	$0.45^{+0.13}_{-0.10}$
Abell 665.....	0.18	181^{+12}_{-11}	$7.4^{+1.6}_{-1.1}$	$3.3^{+0.7}_{-0.6}$	$2.8^{+0.6}_{-0.5}$	$1.55^{+0.89}_{-0.51}$
Abell 697.....	0.28	130^{+13}_{-10}	$8.3^{+2.2}_{-1.5}$	$3.7^{+1.2}_{-0.8}$	$3.2^{+1.0}_{-0.7}$	$0.99^{+0.75}_{-0.38}$
Abell 773.....	0.22	150^{+9}_{-8}	$6.9^{+1.0}_{-0.8}$	$3.1^{+0.6}_{-0.5}$	$2.7^{+0.5}_{-0.4}$	$0.93^{+0.38}_{-0.26}$
CL J0016+1609.....	0.54	81^{+2}_{-3}	$12.6^{+0.9}_{-0.9}$	$4.1^{+0.4}_{-0.5}$	$3.5^{+0.3}_{-0.4}$	$0.92^{+0.11}_{-0.11}$
CL J1226+3332.....	0.89	53^{+1}_{-2}	$9.2^{+0.5}_{-0.5}$	$3.2^{+0.3}_{-0.3}$	$2.7^{+0.2}_{-0.3}$	$0.27^{+0.04}_{-0.03}$
MACS J0647.7+7015	0.58	72^{+3}_{-3}	$8.6^{+1.1}_{-0.9}$	$3.4^{+0.4}_{-0.4}$	$2.9^{+0.3}_{-0.3}$	$0.38^{+0.12}_{-0.09}$
MACS J1311.0-0310.	0.49	73^{+4}_{-5}	$6.8^{+0.8}_{-0.8}$	$2.4^{+0.4}_{-0.5}$	$2.1^{+0.4}_{-0.4}$	$0.26^{+0.08}_{-0.07}$
MACS J2214.9-1359.	0.48	91^{+2}_{-2}	$10.2^{+0.7}_{-0.7}$	$4.5^{+0.3}_{-0.3}$	$3.9^{+0.3}_{-0.3}$	$0.74^{+0.13}_{-0.12}$
MACS J2228.5+2036	0.41	100^{+3}_{-4}	$11.0^{+1.9}_{-1.4}$	$4.3^{+0.5}_{-0.4}$	$3.7^{+0.4}_{-0.4}$	$1.03^{+0.37}_{-0.27}$
MS 0451.6-0305.....	0.55	84^{+3}_{-3}	$11.3^{+1.2}_{-1.2}$	$4.7^{+0.4}_{-0.4}$	$4.1^{+0.4}_{-0.4}$	$0.79^{+0.21}_{-0.16}$
MS 1137.5+6625.....	0.78	49^{+2}_{-3}	$6.4^{+0.4}_{-0.4}$	$1.9^{+0.2}_{-0.3}$	$1.6^{+0.2}_{-0.3}$	$0.12^{+0.02}_{-0.02}$
MS 1358.4+6245.....	0.33	99^{+4}_{-5}	$6.4^{+0.9}_{-0.6}$	$2.4^{+0.3}_{-0.3}$	$2.1^{+0.3}_{-0.3}$	$0.40^{+0.12}_{-0.09}$
RX J1347.5-1145.....	0.45	108^{+4}_{-4}	$12.7^{+1.1}_{-1.0}$	$6.5^{+0.7}_{-0.6}$	$5.6^{+0.6}_{-0.6}$	$1.41^{+0.32}_{-0.27}$
RX J2129.7+0005...	0.24	123^{+9}_{-24}	$7.9^{+3.9}_{-2.1}$	$2.1^{+0.5}_{-1.0}$	$1.8^{+0.4}_{-0.9}$	$0.80^{+0.56}_{-0.35}$
ZW 3146.....	0.29	128^{+6}_{-6}	$8.3^{+1.0}_{-0.9}$	$3.9^{+0.6}_{-0.5}$	$3.3^{+0.5}_{-0.4}$	$0.94^{+0.31}_{-0.24}$

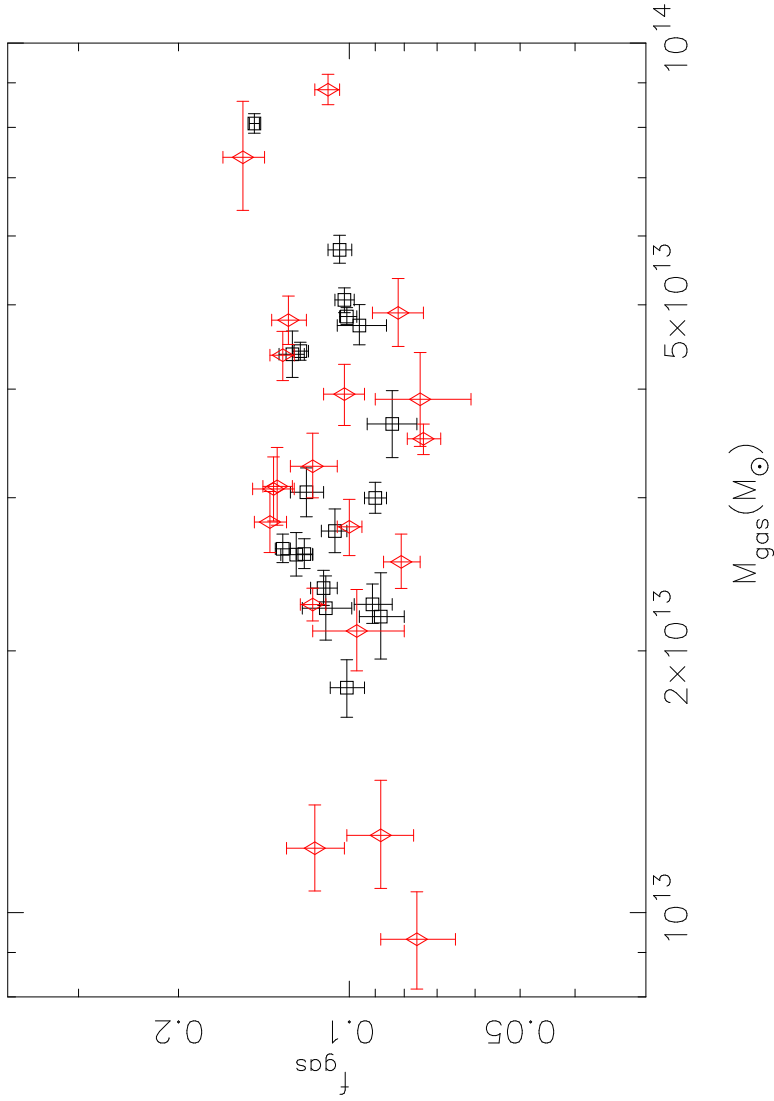


Fig. 1.— Dependence of f_{gas} on M_{gas} ; open squares (in black) are clusters at $0.14 \leq z \leq 0.30$, open diamonds (in red) are clusters at $0.30 < z \leq 0.89$. The gas fraction at r_{2500} shows no evidence of evolution with mass for the clusters in this sample.

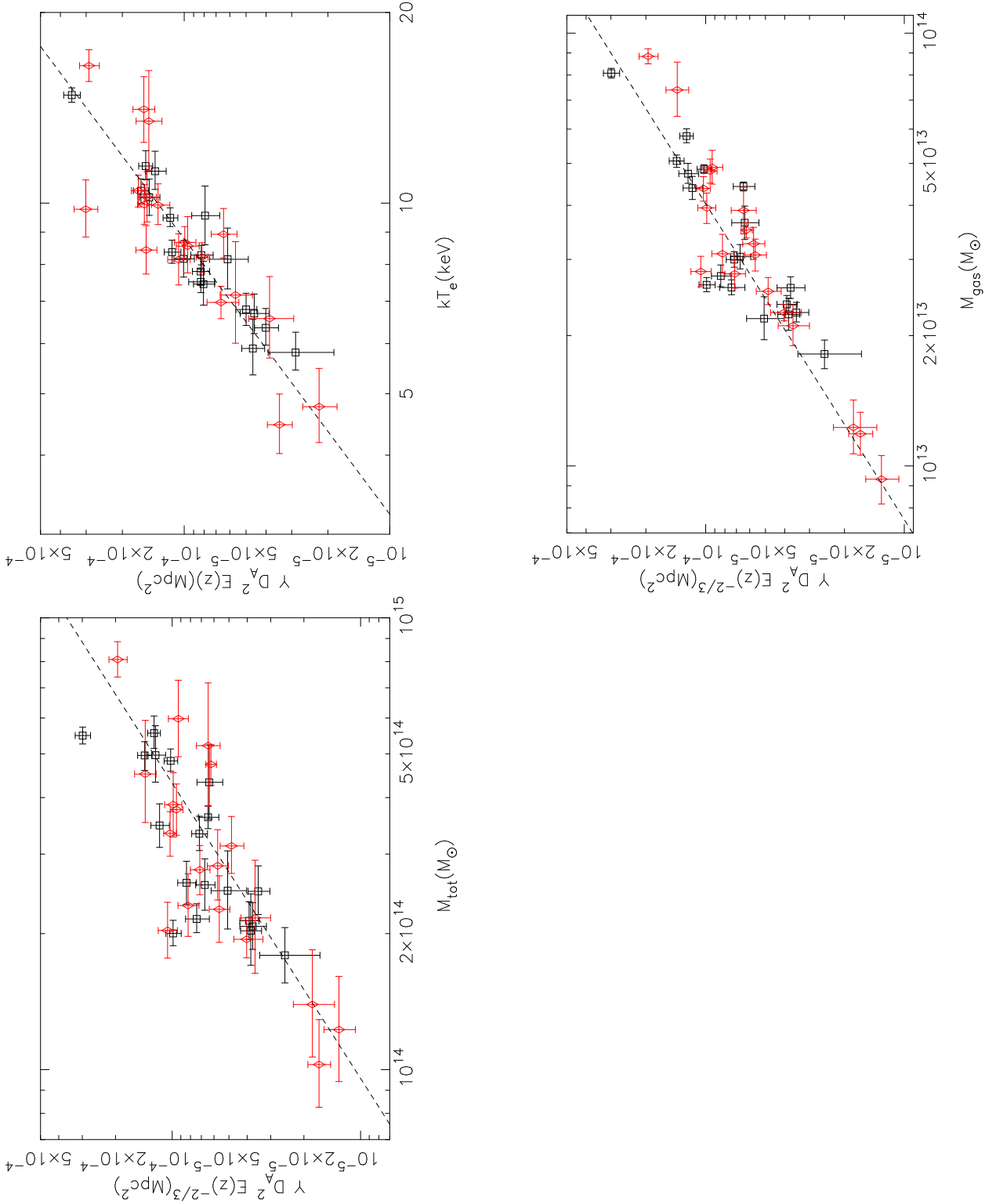


Fig. 2.— Scaling relations between the SZE Y and M_{gas} , M_{tot} and kT_e . Open squares (in black) are clusters at $0.14 \leq z \leq 0.30$, open diamonds (in red) are clusters at $0.30 < z \leq 0.89$. All measurements follow simple power-law models with indices that are consistent with the values of the self-similar scaling theory (Table 1).

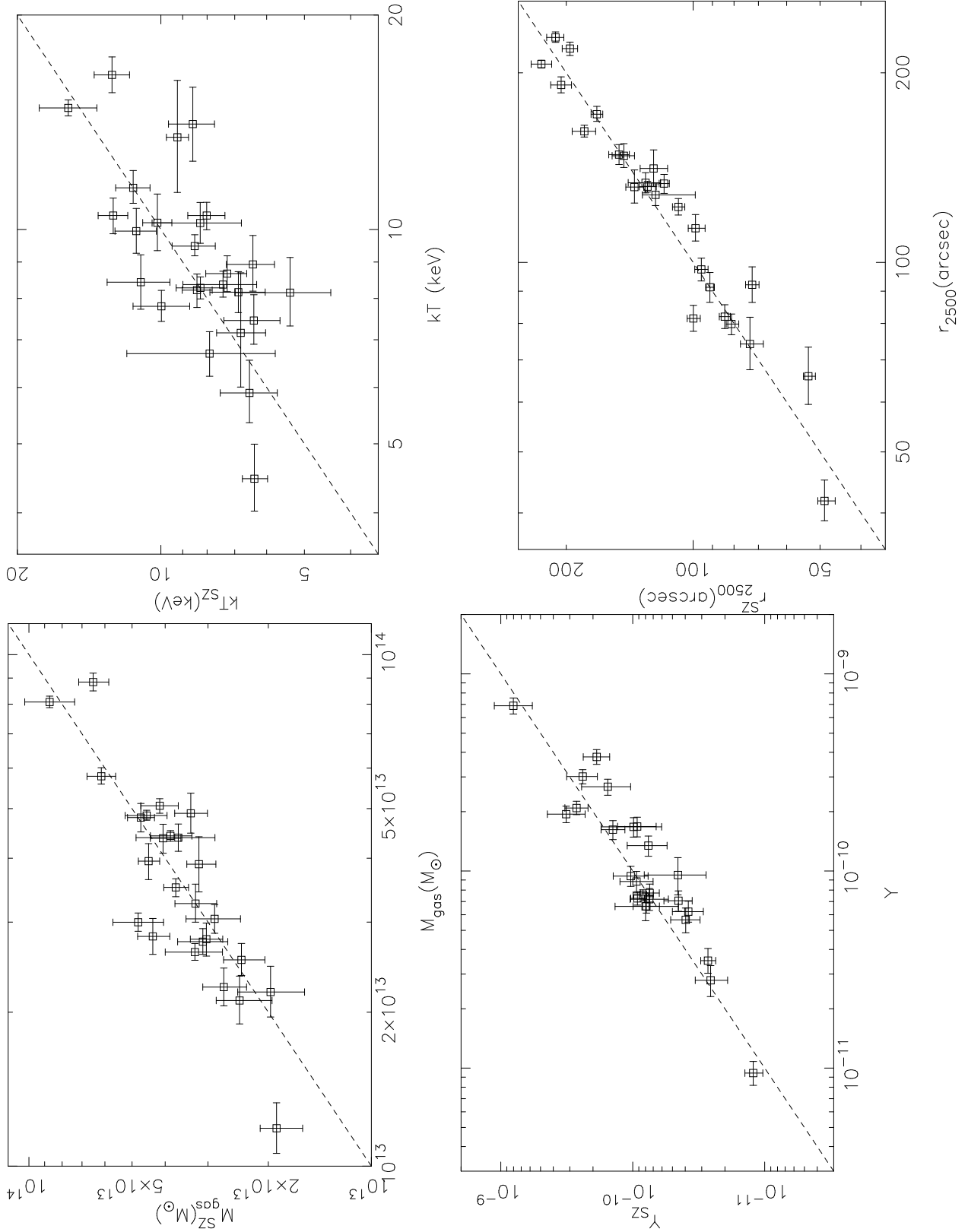


Fig. 3.— Comparison between cluster parameters derived from joint analysis of X-ray and SZE data (x axis) and those derived from SZE data (y axis) following the procedure of Section 5. Dashed lines correspond to $y = x$.

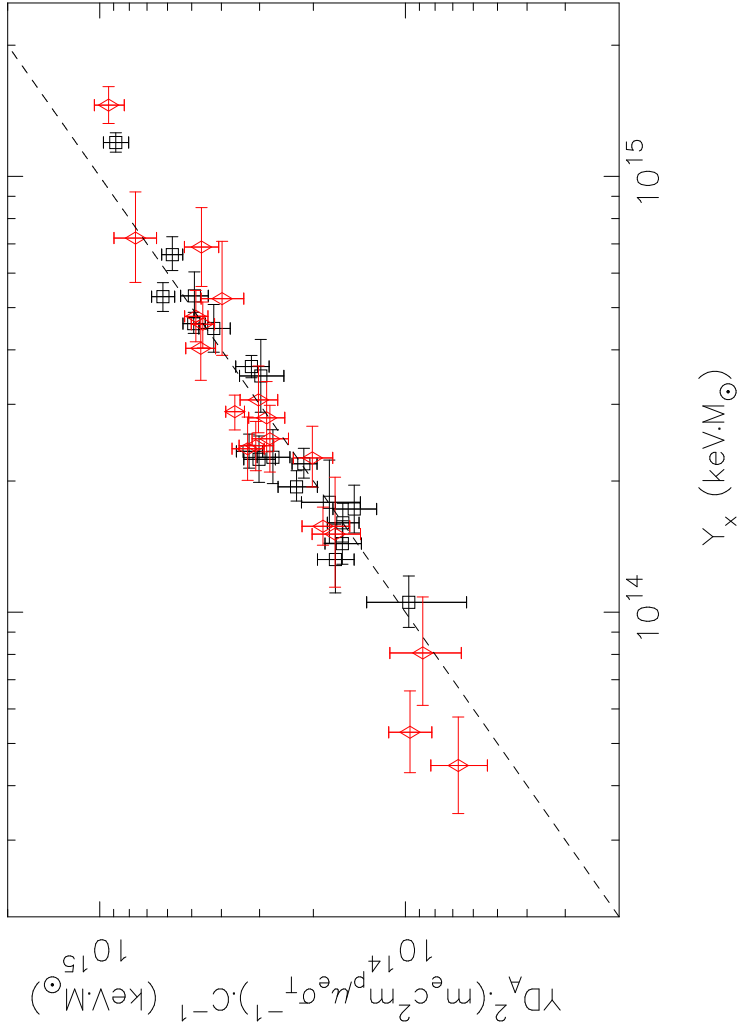


Fig. 4.— Comparison between the SZE Y parameter and the X-ray quantity Y_X (see Section 5 for explanation of the normalization constant); open squares (in black) are clusters at $0.14 \leq z \leq 0.30$, open diamonds (in red) are clusters at $0.30 < z \leq 0.89$. The dashed black line corresponds to $y = x$.

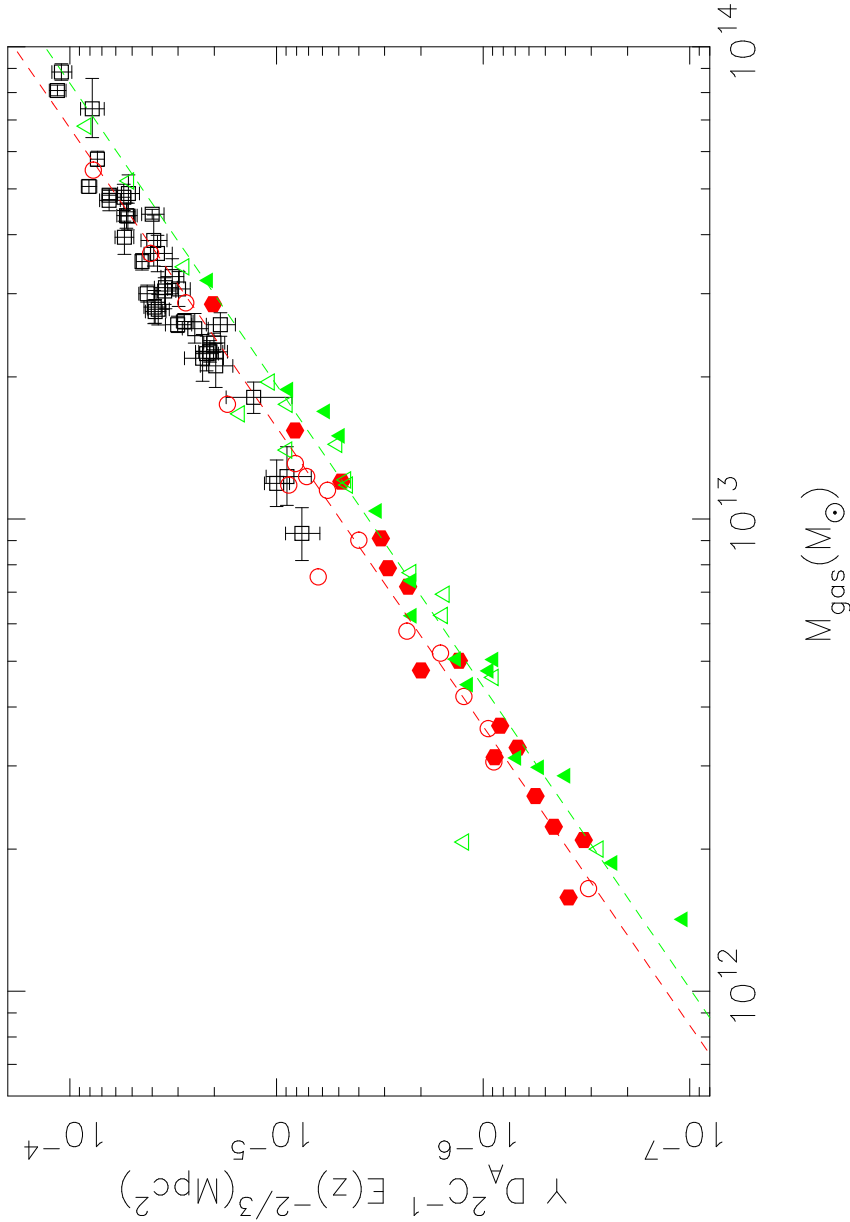


Fig. 5.— M_{gas} vs. Y for simulated and observed clusters. Open squares (in black) are OVRO/BIMA/Chandra measurements. Also shown are simulated clusters from a cooling and star-formation feedback model (red circles) and simulated clusters from a non-radiative model (green triangles) from Nagai (2006). For comparison, all of the M_{gas} and Y quantities are integrated over a spherical volume, as described in Section 5. Open symbols represent simulated clusters at $z=0$ and filled symbols represent simulated clusters at $z=0.6$. The power-law fits to the simulated clusters (dashed lines) are $A = -25.83 \pm 0.52$, $B = 1.58 \pm 0.04$ for the cooling/star-formation model and $A = -25.79 \pm 0.80$, $B = 1.56 \pm 0.06$ for the non-radiative model.